J. Fluid Mech. (2024), *vol*. 999, A23, doi:10.1017/jfm.2024.717

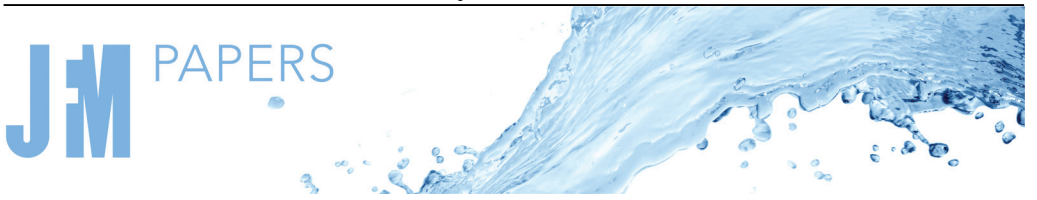

Internal gravity waves in flow past a bluff body under different levels of stratification

D. Gola[1], **S. Nidhan**[1] **and S. Sarkar**[1],†

[1]Department of Mechanical and Aerospace Engineering, University of California San Diego, CA 92093, USA

(Received 27 December 2023; revised 29 May 2024; accepted 4 July 2024)

The flow field of a bluff body, a circular disk, that moves horizontally in a stratified environment is studied using large-eddy simulations. Five levels of stratification (body Froude numbers of $Fr = 0.5$, 1, 1.5, 2 and 5) are simulated at Reynolds number of $Re = 5000$ and Prandtl number of $Pr = 1$. A higher $Re = 50\,000$ database at $Fr = 2$, 10 and $Pr = 1$ is also examined for comparison. The wavelengths and amplitudes of steady lee waves are compared with a linear-theory analysis. Excellent agreement is found over the entire range of Fr if an 'equivalent body' that includes the separation region is employed for the linear theory. For asymptotically large distances, the velocity amplitude varies theoretically as Fr^{-1} but a correction owing to the dependence of the separation zone on Fr is needed. The wake waves propagate in a narrow band of angles with the vertical, and have a wavelength that increases with increasing Fr. The envelope of wake waves, demarcated using buoyancy variance, exhibits self-similar behaviour. The higher Re results are consistent with the buoyancy effects exhibited at the lower Re. The wake wave energy is larger at $Re = 50\,000$. Nevertheless, independent of Fr and Re, the ratio of the wake wave potential energy to the wake turbulent energy increases to approximately 0.6–0.7 in the non-equilibrium stage showing their energetic importance besides suggesting universality in this statistic. There is a crossover of energetic dominance of lee waves at $Fr < 2$ to wake-wave dominance at $Fr \approx 5$.

Key words: stratified flows, stratified turbulence, wakes

1. Introduction

1.1. *Internal waves and their impact*

Relative motion between a submerged body and its stratified environment gives rise to different types of internal gravity waves. Observations of these waves in the ocean and the

† Email address for correspondence: ssarkar@ucsd.edu

atmosphere prompted the first studies of these waves in the geophysical context. Flow over mountains gives rise to lee waves that can lead to changes in properties of air, sometimes visualised as wave clouds. In the ocean, substantial energy is transferred from impinging mean currents and tides at bottom topography to internal waves, e.g. Garrett & Kunze (2007), which, through nonlinear processes break down to turbulence, e.g. Sarkar & Scotti (2017), and the associated turbulent mixing provides an important control on ocean stratification and currents, e.g. Wunsch & Ferrari (2004). The motivating application – bodies moving in a stratified environment – of the present work is different. Here, the body generates lee waves, which are steady in the reference frame of the body, and the unsteady motions in the wake also generate waves (unsteady in the frame of the body). Characterisation of the space–time structure and energetics of these waves is of interest as is quantification of their relationship with the wake and the body generator.

The internal or body Froude number, $Fr = U/ND$, is the important overall parameter that governs internal gravity waves and buoyancy effects on wake dynamics. Here, the density-stratified background is characterised by the buoyancy frequency N where $N^2 = -(g/\rho_0)\partial\rho_b/\partial z$, the relative velocity between the body and the ambient by U and the size of the body by D. In geophysical flows, Fr is generally less or much less than $O(1)$, while in engineering applications (underwater submersibles, aerial vehicles, wind farms, marine turbines) $Fr \geqslant O(1)$.

1.2. *Lee wave studies in the laboratory and with simulations*

Laboratory experiments of stratified flow past a model hill (Hunt & Snyder 1980) and model ridges (Castro, Snyder & Marsh 1983) have characterised lee waves through extensive flow visualisation. Chomaz, Bonneton & Hopfinger (1993) experimentally studied and classified the change of near-wake structure of a sphere wake in uniform stratification as Fr is decreased from greater-than to less-than $O(1)$ values. In a companion study, Bonneton, Chomaz & Hopfinger (1993) described wave characteristics on horizontal planes above the wake using isopyncal displacement inferred from fluorescent dye images. Non-uniform stratification was treated by Robey (1997) who, using experiments and numerics, found the wave field of a sphere moving at the base of a thermocline to be composed of discrete modes that give rise to horizontal-plane patterns reminiscent of Kelvin wakes on the air–sea boundary. Recently, Meunier *et al.* (2018) investigated the wave field of bodies of different shapes and determined how the wavelength and velocity amplitude of lee waves varied with Fr. They also proposed a model for lee wave amplitude that involves modelling the drag as a point force in the Navier–Stokes equations.

Various numerical simulations have also described these lee waves and their effects on the flow at the body and in the wake. For a sphere at $Re = 200$, Hanazaki (1988) found that lee waves suppress separation on decreasing Fr when $Fr > 1$ but induce separation on decreasing Fr when $Fr < 1$. Lee waves lead to oscillatory modulation of the wake width and velocity (Pal *et al.* 2017) and also, near the body, lead to a local minimum of the wake defect velocity at $Nt = \pi$ corresponding to the half-wavelength of the lee wave (Chongsiripinyo & Sarkar 2020). Here, $Nt = Nx/U = x/(FrD)$ converts distance behind the body to time in buoyancy units. Lee waves have a stronger effect on the wake of a slender body, i.e. large value of aspect ratio (AR) given by L/D where L is the length of the body. When the half-wavelength of the lee wave matches L, a condition that is realised at a critical value of $Fr_c = AR/\pi$, the wave leads to maximal contraction of the separated flow at the trailing edge. Thus, in a large-eddy simulations (LES) study (Ortiz-Tarin, Chongsiripinyo & Sarkar 2019) of flow past a 4 : 1 spheroid at $Re = 10^4$,

the wake which was turbulent at high Fr exhibited strong suppression of wake turbulence at $Fr = 1$. The problem of a disk at $Re = 5000$ in nonlinear stratification with minimum $Fr = 1$ was studied by Gola *et al.* (2023). Linear theory (Voisin 1991, 2003, 2007) was used with an equivalent body comprising of the disk and its separation bubble and found to predict the wave amplitude of a single test case ($Fr = 1$) with linear stratification but not the nonlinearly stratified cases. In the present work, lee waves in linear stratification will be characterised over a wide range of Fr and the applicability of linear theory will be evaluated.

1.3. *Evolution of stratified turbulent wakes*

Turbulent stratified wakes exhibit a stark contrast in the evolution of their deficit velocity and length scales relative to their unstratified counterpart. Although the present focus is on internal waves, previous work in this area is briefly summarised for completeness.

Several experimental studies (Lin & Pao 1979; Lin, Boyer & Fernando 1992; Spedding, Browand & Fincham 1996; Spedding 1997; Bonnier & Eiff 2002) have reported significant buoyancy effects on the evolution of wake thickness and/or wake deficit in the flow behind a horizontally moving sphere. Spedding (1997) found that the decay of the wake deficit velocity is characterised by three stages: the near wake regime; the non-equilibrium (NEQ) regime, where the wake decay rate is reduced as it adjusts to the surrounding stratification; and the quasi-two-dimensional regime, where pancake vortices form and the wake decay speeds up. The transition between stages occurred at nominally fixed values of Nt. In another laboratory study, Spedding (2001) showed that stratification biases turbulence towards a faster decay of the vertical fluctuations as compared with the horizontal fluctuations.

Numerical investigations of the problem started with a temporal model (Gourlay *et al.* 2001) where the wake is simulated in a frame moving with the body, a streamwise periodic domain is used and flow statistics evolve in time. The model does not include the wake generator and is instead initialised with a flow field that approximates experimentally observed mean velocity and turbulence intensities at some distance from the body. Since the boundary layer on the body and the small scales in the near wake do not need to be resolved, the temporal model has the advantage that the simulated flow can progress into the late wake with reasonable computational cost. The limitations are that the absence of the wake generator excludes lee waves and their influence on the wake as well as vortex shedding from the body. Also, temporal models are sensitive to initial flow conditions (Redford, Castro & Coleman 2012). The alternative approach of body-inclusive simulations will be adopted here.

The multistage decay of the wake has been studied numerically using temporal models (Gourlay *et al.* 2001; Dommermuth *et al.* 2002; Brucker & Sarkar 2010; Diamessis, Spedding & Domaradzki 2011; de Stadler & Sarkar 2012; Zhou & Diamessis 2019). The anisotropy created by stratification suppressing vertical fluctuations leads to decreased turbulent production in the wake (Brucker & Sarkar 2010), leading to the longer lifespan of the stratified wake, a result that is supported by Redford, Lund & Coleman (2015) in their direct numerical simulations (DNS) of a weakly stratified turbulent wake. The buoyancy-induced decrease in the correlation coefficient between vertical and horizontal fluctuations is a generic feature of stratified shear flows and was identified by Jacobitz, Sarkar & VanAtta (1997) in homogenous shear flow and also by others in following studies of a variety of shear flows.

In recent times, body-inclusive simulations, e.g. Orr *et al.* (2015), Pal *et al.* (2017), Ortiz-Tarin *et al.* (2019) and Chongsiripinyo & Sarkar (2020), have been conducted to

increase the realism of simulations. Such an approach captures flow separation, vortex shedding from the body and also the lee waves leading to more accurate representation of the near and intermediate wake. Body inclusive simulations are akin to laboratory experiments by virtue of including the body, while also alleviating the aforementioned limitations of temporal-model simulations. Besides, body-inclusive simulations lead to statistically steady data so that numerical techniques like spectral proper orthogonal decomposition can be fruitfully used to extract wake structures that are statistically space–time coherent, e.g. Nidhan *et al.* (2020) and Nidhan, Schmidt & Sarkar (2022). Reaching beyond $x/D = O(100)$ in body-inclusive simulations is computationally too expensive but this issue can be overcome by a hybrid simulation technique that continues the flow to larger x/D (equivalently Nt) in a follow-up simulation that uses a temporal model (Pasquetti 2011) or a spatial model (VanDine, Chongsiripinyo & Sarkar 2018) with a coarser grid that needs to resolve only the large length scales of the far wake.

1.4. *Wake waves and their link to wake structures*

Wake waves are internal waves forced by the unsteady fluctuations in the turbulent wake. The first report of stratified wake waves was by Gilreath & Brandt (1985) who observed 'short, random' unsteady waves in their experiments with a streamlined body in towed and self-propelled modes. Besides uniform stratification, they also considered a pycnocline to find solitary internal wave propagation at low Fr. Bonneton *et al.* (1993) distinguished wake waves from lee waves and, by spectral analysis of density-probe measurements, linked these waves to coherent wake structures. Robey (1997) linked the wake waves to the size of large-scale structures in the wake. Towed sphere experiments by Brandt & Rottier (2015) showed that lee waves dominate in the $Fr \lesssim 1$ regime while wake waves dominate in the $Fr \gtrsim 1$ regime. They also provide a qualitative estimate of the total potential energy that was found to scale as Fr^2. The recent work of Meunier *et al.* (2018) considered wake waves in addition to lee waves and quantified the dependence of their wavelength and velocity amplitude on Fr.

Abdilghanie & Diamessis (2013) conducted a comprehensive study of the internal wave field of a stratified turbulent wake using temporal simulations for a wide range of Re and found that, at higher Re, there is a broader range of wave propagation angles (40°–55°), at least at early Nt, relative to lower values of Re. Brucker & Sarkar (2010) studied towed and self-propelled wakes using temporal simulations at $Re = 5 \times 10^4$ and various Fr. They concluded that internal wave flux dominated the turbulent dissipation in the wake kinetic energy budget for $20 < Nt < 75$. This was also supported by Rowe, Diamessis & Zhou (2020) who, in their temporal-model simulations over a broad range of Re and Fr, found that internal wave radiation is an important sink for wake kinetic energy after $Nt = 10$. Indeed, the energetic importance of internal waves for turbulence in stratified shear flows is a more general result in view of such demonstrations for a shear layer (Pham, Sarkar & Brucker 2009; Watanabe *et al.* 2018) and a boundary layer (Taylor & Sarkar 2007).

1.5. *Objectives of present study*

Body-inclusive simulations capture lee waves as well as wake waves and present an opportunity to characterise and contrast their properties. This motivates the present waves-focussed study of a disk wake in linear stratification at $Re = 5000$.

Our results on scaling laws for Fr dependency of internal waves in turbulent flow past a disk will be compared with previous laboratory experiments and, for wake waves, also with body exclusive temporal model simulations. The skill of linear theory in predicting

lee waves will be assessed. The internal wave field in cases from a recent study of disk wakes at an order of magnitude larger $Re = 50\,000$ that focussed on wake decay laws will also be analysed.

The specific questions that we intend to answer as stratification is varied parametrically for a turbulent wake are as follows. (i) How does linear theory applied to an equivalent body, an approach which was shown to predict body-generated lee waves in a turbulent disk wake at a single $Fr = 1$, work over the range of Fr considered here? For example, how do linear theory results, $w \propto Fr^{-1}$ scaling of the amplitude and $\Lambda = 2\pi FrD$ scaling of wavelength, compare with the simulation results? (ii) How do internal wave structural properties (phase angle, wavelength, spatial distribution) change as a function of Fr? Are there scaling laws for the Fr dependence? (iii) There is fluctuation energy in the turbulent wake and also outside it in the form of internal waves. How are kinetic and potential energy partitioned between the wake and wave field? How does the energy in wake waves compare with that in lee waves? (iv) Are results for the two cases at higher $Re = 50\,000$ consistent with trends exhibited in the parametric study at the lower value of $Re = 5000$?

A disk is used as the wake generator in body-inclusive LES, the numerics of which are laid out in § 2. Lee waves and their dependence on Fr is described in § 3. Characteristics of wake-generated internal gravity waves are described in § 4. Energy partition of the entire flow field is done to calculate the energies associated with lee waves, wake waves, mean wake and turbulent wake, and their variation with Fr is analysed in § 5. The influence of Reynolds number is briefly assessed in § 6. To conclude, a summary and a discussion are presented in § 7.

2. Methodology

2.1. *Governing equations and numerical scheme*

The wake of a disk is simulated for five different cases of stratification by solving the three-dimensional, incompressible, unsteady form of the conservation equations for mass, momentum and density. A high-resolution LES with the Boussinesq approximation for density effects is used. The disk, with diameter D and thickness $0.01D$, is immersed perpendicular to a flow with velocity U_∞. The equations are numerically solved in cylindrical coordinates but both Cartesian (x, y, z) and cylindrical (r, θ, x) coordinates are used as appropriate in the discussion. Here, x is streamwise, y is spanwise and positive along $\theta = 0^\circ$ and z is vertical and positive along $\theta = 90^\circ$ (figure 1). The density field $(\rho(\boldsymbol{x}, t))$ is split into a constant reference density (ρ_0), the variation of the background $(\Delta\rho_b(z))$ and the flow induced deviation, $(\rho_d(\boldsymbol{x}, t))$ so that $\rho(\boldsymbol{x}, t) = \rho_0 + \Delta\rho_b(z) + \rho_d(\boldsymbol{x}, t)$. The Reynolds number of the flow, defined as $Re = U_\infty D/\nu$ is 5000. The different levels of stratification are quantified by the Froude number, $Fr = U_\infty/ND$, which takes values of 0.5, 1, 1.5, 2 and 5 for the five cases. Here, N is the buoyancy frequency given by $N = \sqrt{(-g/\rho_0)(\partial\Delta\rho_b(z)/\partial z)}$.

The filtered non-dimensional equations, using D, U_∞ and ρ_0 as the characteristic length, velocity and density scales, respectively, are as follows

$$\frac{\partial u_i}{\partial x_i} = 0, \tag{2.1}$$

$$\frac{\partial u_i}{\partial t} + u_j\frac{\partial u_i}{\partial x_j} = -\frac{\partial p}{\partial x_i} + \frac{1}{Re}\frac{\partial}{\partial x_j}\left[\left(1 + \frac{\nu_{sgs}}{\nu}\right)\frac{\partial u_i}{\partial x_j}\right] - \frac{\rho_d}{Fr^2}\delta_{i3}, \tag{2.2}$$

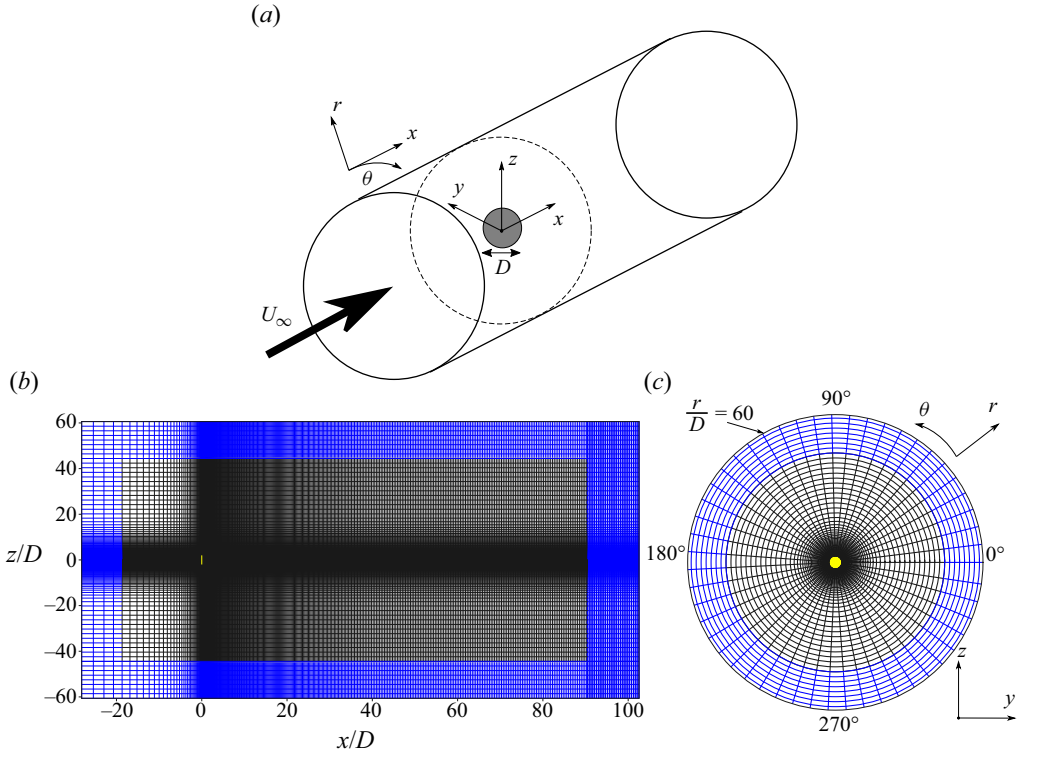

Figure 1. (*a*) Schematic showing the simulation set-up and domain. (*b*) Radial and streamwise grids visualised on the $y = 0$ plane. (*c*) Radial and azimuthal grids visualised on the $x = 0$ plane. (Every fifth gridline is shown, with blue lines representing the sponge region. Disk (not to scale) is shown in yellow.)

$$\frac{\partial \rho}{\partial t} + u_j \frac{\partial \rho}{\partial x_j} = \frac{1}{RePr} \frac{\partial}{\partial x_j} \left[\left(1 + \frac{\kappa_{sgs}}{\kappa} \right) \frac{\partial \rho}{\partial x_j} \right], \tag{2.3}$$

where u_i refers to the filtered non-dimensional velocities in the cartesian coordinate system for $i = 1, 2$ and 3, respectively. The Smagorinsky eddy viscosity model with dynamic procedure (Germano *et al.* 1991) is employed to obtain ν_{sgs} wherein, the coefficient C in the expression $\nu_{sgs} = C\tilde{\Delta}^2|\tilde{S}|$ ($\tilde{\Delta}^3$ being the cell volume and $|\widetilde{S}|$ being the strain rate magnitude) is obtained dynamically using the least squares approach of Lilly (1992) and the Lagrangian averaging method of Meneveau, Lund & Cabot (1996). The Lagrangian averaging method takes the cumulative average of C as a function of time, with more weight assigned to recent times in flow evolution. The Prandtl number ($Pr = \nu/\kappa$) as well as the subgrid Prandtl number ($Pr = \nu_{sgs}/\kappa_{sgs}$) is set to unity. Second-order central finite difference is used in space. A low storage third-order Runge–Kutta scheme for the advective terms and a Crank–Nicolson term for the viscous terms are used to advance the solution in time. The disk is represented using the immersed boundary method of Balaras (2004) and Yang & Balaras (2006).

2.2. *Domain and statistics*

The domain extends from $x/D = -L_x^- = -30$ to $x/D = L_x^+ = 102$ in the streamwise direction and from $r/D = 0$ to $r/D = L_r = 60$ in the radial direction (figure 1*b*,*c*). The

number of grid points in the streamwise, azimuthal and radial directions are $N_x = 2176$, $N_\theta = 256$ and $N_r = 479$. The disk surface is resolved into 47 312 triangles to identify the fluid–solid interface. The streamwise and radial grids in the flow solver are structured and employ uniform stretching as distance from the disk increases. There are 73 points along the disk in the radial direction. Maximum values of $\Delta x/\eta$ and $\Delta r/\eta$, where $\eta = (\nu^3/\varepsilon)^{1/4}$ is the Kolmogorov length scale, are used to ascertain adequate grid resolution. The chosen grid has $(\Delta x/\eta)_{max} = 4.84$ and $(\Delta r/\eta)_{max} = 5.43$ across all cases. The grid in the azimuthal direction is homogenous. Owing to the high grid resolution, the subgrid viscosity (ν_{sgs}) is not large. The instantaneous maximum value of subgrid viscosity fluctuates between $\nu_{sgs}/\nu = 2.5$ and $\nu_{sgs}/\nu = 5$ after statistical stationarity is achieved. The location of this maximum value is $0.5 < r/D < 1.5$ and $0 < x/D < 2$. Beyond $x/D = 10$, $\nu_{sgs}/\nu < 1$. Statistics are collected by temporal averaging after the initial transient has subsided and statistical steady state has been reached. The time interval for averaging is $140D/U_\infty$. For any dependent variable in the simulation, $\langle . \rangle$ represents the time average and superscript $'$ represents the fluctuation about that average. From this section onwards, all the variables will appear in their dimensional form and any non-dimensionalisation will be explicitly shown, e.g. x/D or w/U_∞.

2.3. *Boundary conditions*

For boundary conditions, the inlet ($x/D = -30$) has a uniform free stream of magnitude U_∞ in the positive x direction, the outlet ($x/D = 102$) has an Orlanski-type convective boundary condition (Orlanski 1976), and the radial boundary ($r/D = 60$) has a Neumann boundary condition for density as well as velocity. The centreline boundary ($r = 0$) is handled by taking the average of the two symmetrically located ghost cells over the centreline to define the radial and azimuthal velocity components at the centreline. To prevent spurious reflection of waves back into the domain, sponge layers are used at the three boundaries of the computational domain. The radial sponge starts at $r/D = 45$ and goes up to the radial boundary $r/D = 60$, the inlet sponge is from $x/D = -30$ to $x/D = -20$ and the outlet sponge is from $x/D = 90$ to $x/D = 102$. Each of the sponge layers use a quadratic damping function of the form $f_{damp} = C((x - x_{spng})/(L_x - x_{spng}))^2(\phi_0 - \phi(x))$, where the variable $\phi(x)$ is relaxed to the target value ϕ_0 in the sponge layer given by $x_{spng} < x < L_b$. For example, in the radial sponge, where x in $f_{damp}(x)$ is equivalent to r, the sponge begins at $r_{spng}/D = 45$ and extends up to $L_r/D = 60$, and the strength of the damping function is $C = 5$.

3. Body-generated lee waves

In stratified environments, the wave component of the flow field consists of body-generated lee waves and wake-generated internal waves. The former is steady in time with respect to the body while the latter is unsteady. Figure 2 illustrates these two types of waves for the five values of Froude number by plotting the vertical velocity at the top half of the vertical centreplane. The steady lee waves are seen as the large band of waves spanning most of the domain while the unsteady waves are seen as a radially thinner band of irregular waves superposed on the lee waves. Gola *et al.* (2023) studied the steady lee waves generated by a disk at $Re = 5000$ focussing on how nonlinear stratification (pycnocline) as well as the relative position of the pycnocline with respect to the disk modifies the flow. The minimum background Froude number for the pycnocline cases was $Fr = 1$ as was the constant value of Fr in the linearly stratified baseline case.

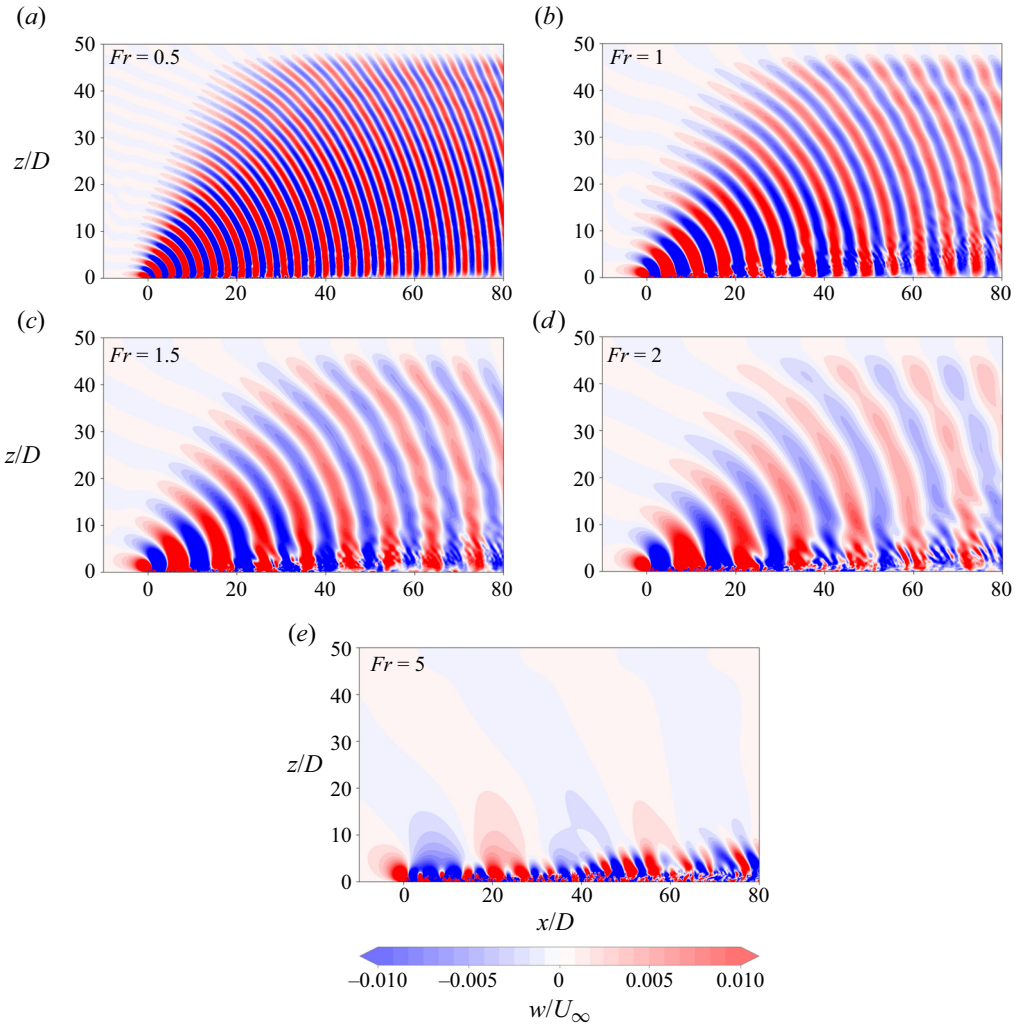

Figure 2. Instantaneous contours of vertical velocity showing body-generated lee waves (steady in the simulation frame) on the $\theta = 90^\circ$, vertical centreplane for the five cases.

For the steady lee waves, Gola *et al.* (2023) found that the wavelength in all cases and the amplitude in the linearly stratified $Fr = 1$ case could be deduced from the linear theory (with the value of N in the far field where waves propagate) given by Voisin (1991, 2003, 2007) and by modelling the disk plus its separation bubble as one body, specifically a Rankine ovoid. The potential flow past an ovoid is given by the superposition of a doublet (source/sink of strength $\pm m$ separated by distance of $2a$) and the uniform incident flow. The expression for the vertical velocity deduced by Ortiz-Tarin *et al.* (2019) after adapting the linear theory to an ovoid-shaped body is

$$w(x, y, z) \sim -\frac{mN}{\pi U_\infty r_{xyz}} \sin\theta \cos\psi (1 + \cot^2\psi \cos^2\theta)^{1/2} \sin\left(\frac{Na}{U_\infty} \cos\psi |\sin\theta|\right) \times \sin\left(\frac{N}{U_\infty} r_{xyz} |\sin\theta|\right), \tag{3.1}$$

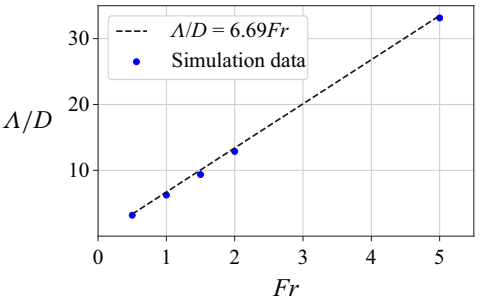

Figure 3. Wavelength of body-generated lee waves.

where $r_{xyz} = \sqrt{x^2 + y^2 + z^2}$, $\psi = \arctan(\sqrt{y^2 + z^2}/x)$ and $\theta = \arctan(z/y)$ is the azimuthal angle in figure 1. Specialisation to the $y = 0$ plane leads to

$$w(x, y = 0, z) \sim -\frac{mN}{\pi U_\infty r_{xz}} \cos\psi \sin\left(\frac{Na}{U_\infty}\cos\psi\right) \sin\left(\frac{N}{U_\infty} r_{xz}\right), \tag{3.2}$$

where $r_{xz} = \sqrt{x^2 + z^2}$ and $\psi = \arctan(z/x)$. The theoretical result, (3.2), will be subsequently compared with the simulation results.

As in the $Fr = 1$ case tested by Gola *et al.* (2023), m and a are calculated here from the potential-flow solution for a Rankine ovoid of length L_{ro} and cross-sectional diameter D_{ro} fitted using the streamline $\langle u \rangle = 0.95U_\infty$:

$$(L_{ro}^2 - 4a^2)^2 = \left(\frac{8ma}{\pi U_\infty}\right) L_{ro}, \quad D_{ro}^2 = \left(\frac{8ma}{\pi U_\infty}\right) \frac{1}{\sqrt{4a^2 + D_{ro}^2}}. \tag{3.3a,b}$$

It can be deduced from the argument of the last sine term in (3.2) that the wavelength of the steady lee waves is $\Lambda/D = 2\pi Fr$. The wavelength of the lee waves obtained from the simulations along the line $x = z$, $y = 0$ is shown in figure 3, wherein it follows the trend $\Lambda = 6.7Fr$, which is close to the asymptotic result of $\Lambda/D = 2\pi Fr$.

Note that (3.1) does not apply to $Fr < O(0.1)$ when the flow is mostly around the disk and the region involved in wave generation shrinks from the crest to the dividing streamline at a depth of approximately U_∞/N from the crest. Thus, the singular limit $Fr \to 0$ of (3.1) is inadmissible.

Figure 4 shows the vertical velocity w for the five cases on the line $z = x$, $y = 0$ as a function of distance from the disk centre, $s = \sqrt{x^2 + z^2}$. Excellent agreement of the simulation results with linear theory, (3.2), is seen. Also plotted alongside in figure 4(*b*) are the defect velocity ($U_d = U_\infty - \langle u \rangle$) contours. There is a case-dependent difference in the separation bubble. The length of the separation bubble increases with increasing Fr leading to a different set of values for m and a in (3.1) for each case. Figure 5 shows the comparison of the vertical velocity contours on the r–θ plane obtained from the simulation and linear theory (3.1) for $Fr = 1$ at $x/D = 10$ and 30. The contours are seen to span a larger area in the r–θ plane as distance from the body is increased. Again, good agreement between the simulation and theory is found. The amplitude of the lee wave (maximum or minimum at $x/D = 20$, $r/D > 10$), which is plotted in figure 6(*a*), reveals excellent agreement between theory and simulation. The w-amplitude of the lee wave in (3.1) is proportional to the product of m and N so that the change in the size of the separation region behind the disk also plays a part in the resulting wave amplitude as is reflected by the dependence of m in (3.1) on Fr (figure 6*b*). This results in a scaling that is different from $w/U_\infty \sim Fr^{-1}$, which would be the case if m were assumed constant across Fr.

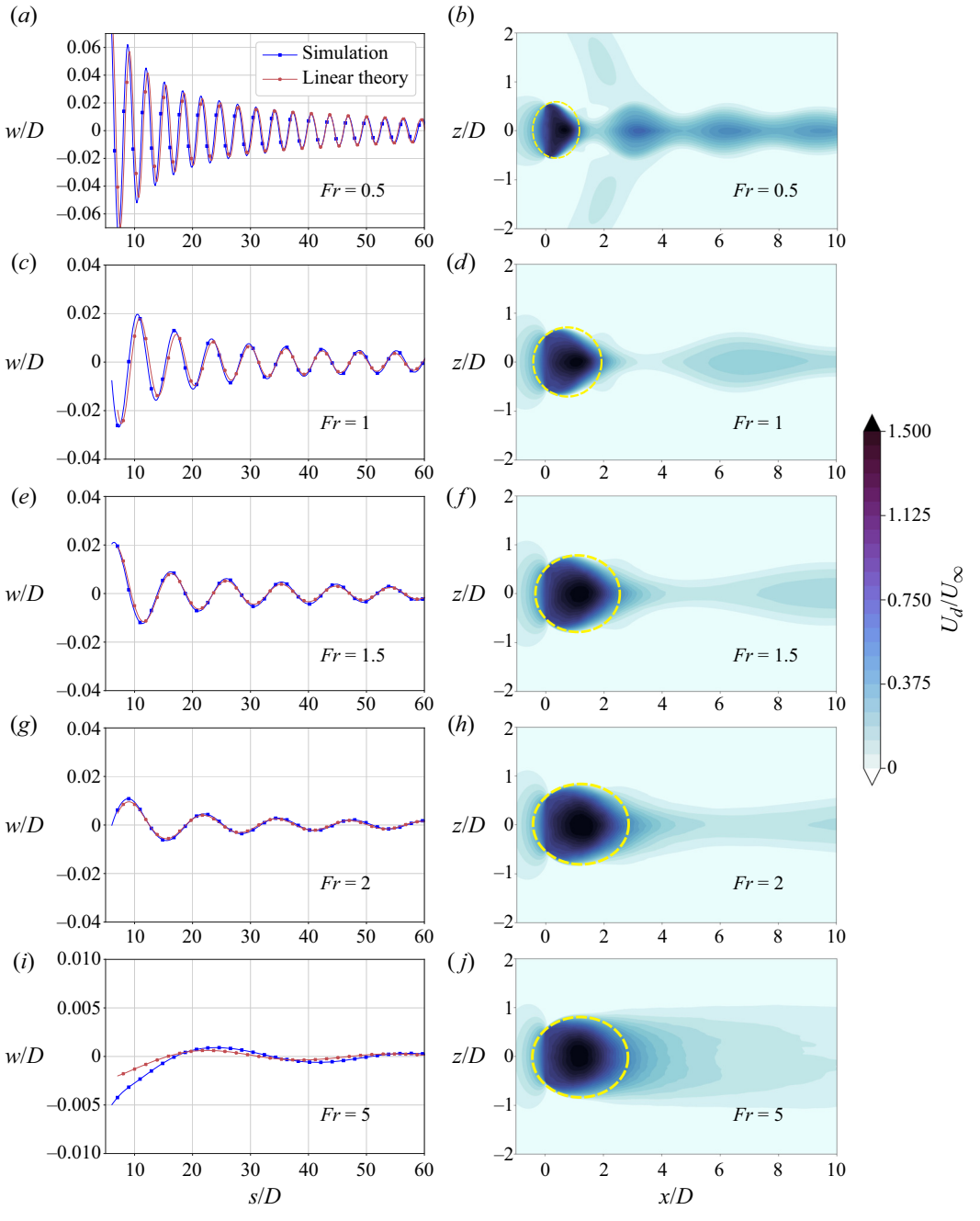

Figure 4. Body-generated lee waves. (*a*,*c*,*e*,*g*,*i*) Vertical mean velocity plotted along the line $z = x, y = 0$ on the top half of the vertical plane ($s = \sqrt{x^2 + z^2}$). (*b*,*d*,*f*,*h*,*j*) Defect velocity (U_d) contours showing the increasing size of the fitted Rankine ovoid (yellow dashed line) with increasing *Fr*.

Meunier *et al.* (2018) obtained the mean horizontal divergence magnitude ($|\partial\langle w\rangle/\partial z|$) of the internal wave field in an experimental study of waves emitted by towing a sphere, 6 : 1 cylinder and 6 : 1 spheroid in a stratified fluid. Measurements of $u(x, y)$ and $v(x, y)$ on a horizontal plane were used to infer $|\partial\langle w\rangle/\partial z|$. For comparison, the mean horizontal

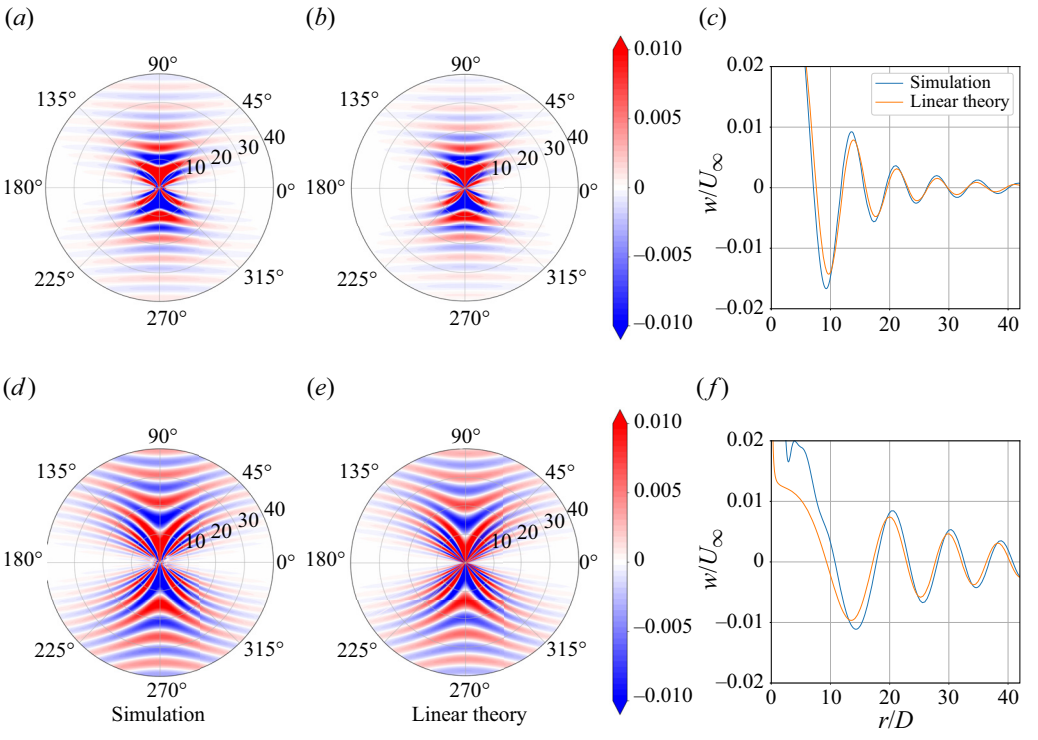

Figure 5. Body-generated lee waves shown at two downstream locations for $Fr = 1$: vertical velocity contours compared with linear theory at $x/D = 10$ (*a–c*) and 30 (*d–f*). Line plots compare w at $\theta = 90°$.

divergence magnitude at the local maxima/minima for w at $x/D = 10$, $r/D = 3$ for the disk simulations is plotted along with the data from Meunier *et al.* (2018) in figure 7. Note that the chosen locations of the maxima/minima in the simulations are somewhat different from those in Meunier *et al.* (2018), reflecting the difference between simulation and experimental methodologies. The simulation results for the disk are comparable to the experimental results of Meunier *et al.* (2018) for other axisymmetric bodies.

4. Wake-generated internal gravity waves

The wake-generated internal waves are manifested in the simulation reference frame as the unsteady component of the wave field. To visualise these waves without their steady counterpart, instantaneous contours of the fluctuation $(\partial w'/\partial z)$ in vertical divergence on the top half of the vertical plane is plotted in figure 8 for all the five cases. In a time series of these contours, these waves are seen to advect downstream (see Supplementary material 'Movie1.mp4' available at https://doi.org/10.1017/jfm.2024.717), unlike the steady lee waves. When viewed in a reference frame moving with the free stream (see Supplementary material 'Movie2.mp4'), these waves move slowly towards the left while growing in the vertical. In other words, the wave phase speed is less than the free stream velocity magnitude.

Across the five cases, three features of these internal waves can be noted: (i) the inclination angle with the vertical (Θ) is in a narrow range (35°–40°), specifically 35°, 39°, 35°, 40° and 37° in the order of increasing Fr; (ii) the wavelength increases with increasing Fr; (iii) the vertical extent of propagation with respect to the body decreases

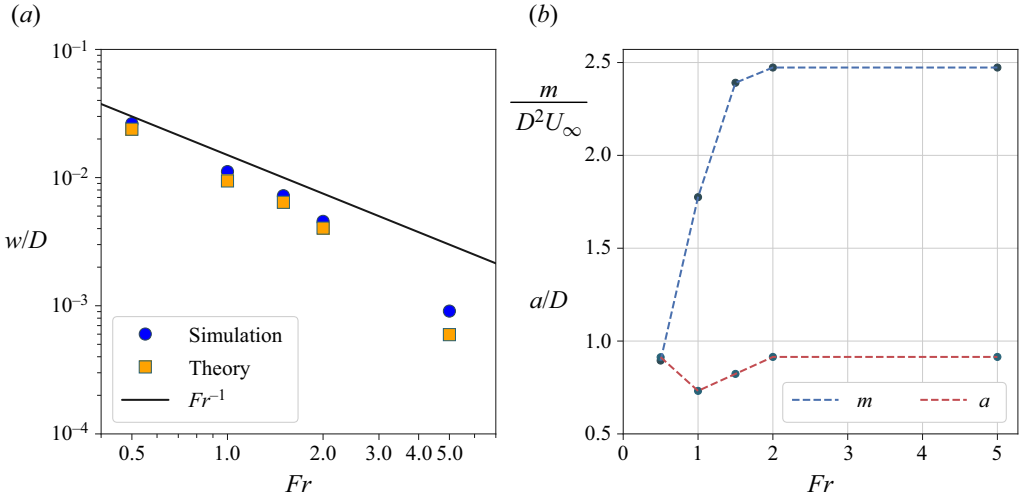

Figure 6. (*a*) Vertical mean velocity magnitude of the lee waves at local maxima/minima near $x/D = 20$ in figure 4(*a*). (*b*) Variation of m and a (obtained by fitting the resulting ovoid to the mean separation bubble) with Fr.

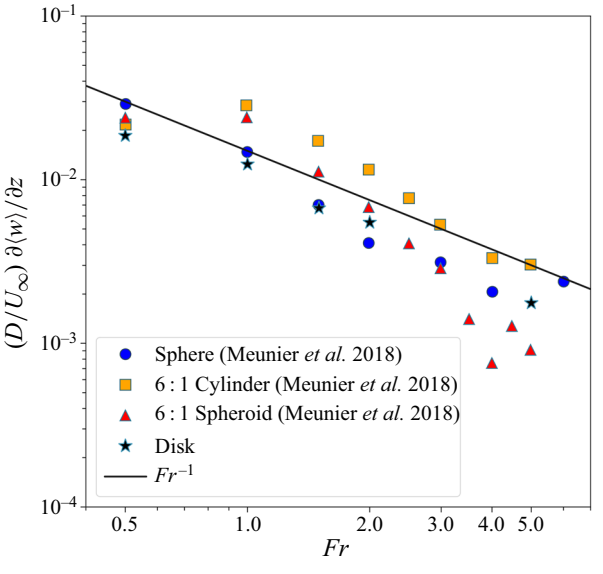

Figure 7. Comparison of mean divergence magnitude of the lee-wave field between the present disk simulation and the laboratory results reported by Meunier *et al.* (2018).

with increasing Fr. The first feature, the clustering of the waves around the same vertical angle, was explained using the argument of maximising the vertical component of group velocity for a fixed horizontal wavenumber by Taylor & Sarkar (2007). The vertical group velocity for internal gravity waves in stratified flow without rotation is given by

$$c_{gz} = -\frac{N}{|\boldsymbol{k}|}\cos\Theta\sin\Theta = -\frac{N}{|k_x|}|\cos\Theta|\cos\Theta\sin\Theta, \tag{4.1}$$

where $|k|$ is the wavenumber magnitude and k_x is the horizontal wavenumber. Note that for our simulations, Θ is an obtuse angle because the waves propagate in the negative x

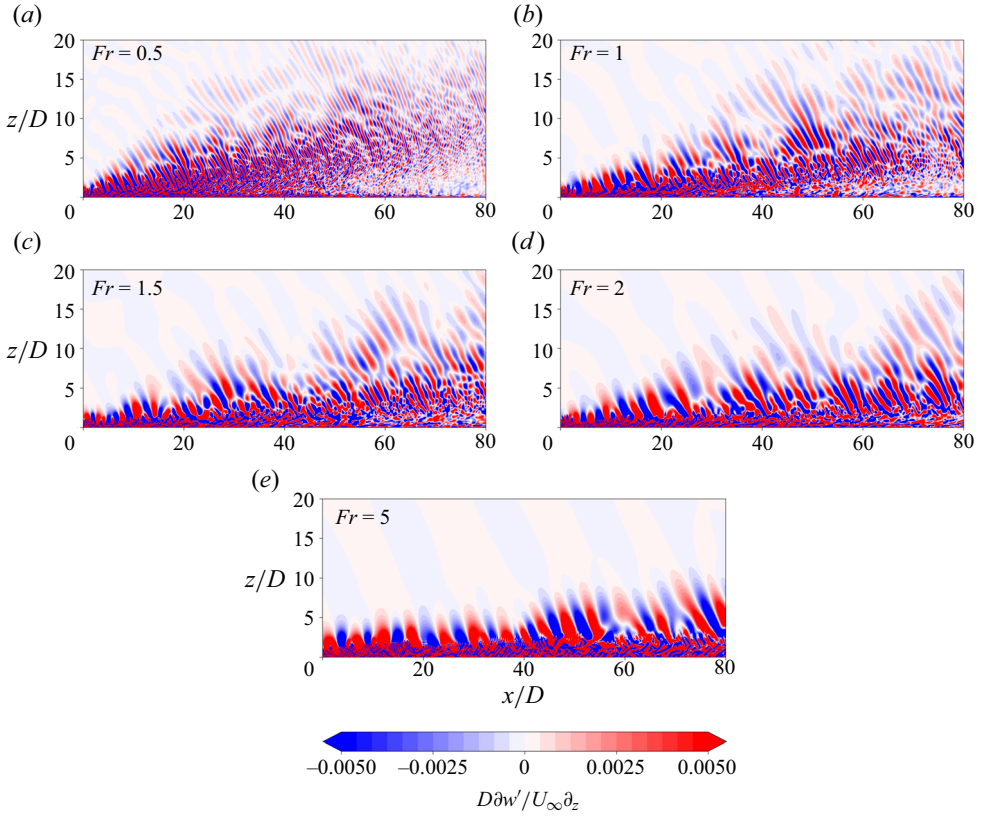

Figure 8. Instantaneous contours of vertical derivative of vertical velocity fluctuation showing wake-generated internal gravity waves on the $\theta = 90^\circ$ plane for the five cases.

direction as discussed earlier. It can be shown that the expression on the right-hand side of (4.1) is maximum when $\Theta \approx 145^\circ$ or 35° from the vertical, which is close to the angles observed in the simulations.

It is evident from figure 8 that the wavelength of the wake waves increases with Fr. This dependence is quantified by computing the wavelength (λ), normalised by D, from wave packets in the instantaneous $\partial w'/\partial z$ fields shown in figure 8. The wave packets are chosen to be 4–5 wavelengths long in the NEQ region away from the wake to avoid turbulence but also close enough to get a strong clean signal (this corresponds to the region $5 < z < 15$, $5 < Nt < 30$ depending on Fr). Figure 9 shows λ plotted against Fr. There is reasonable agreement with the scaling $\lambda \propto Fr^{1/3}$ (dashed line) found by Abdilghanie & Diamessis (2013) and Meunier *et al.* (2018). The horizontal width (L_{Hk}) of the kinetic energy profile of the disk wake varies as $L_{Hk} \propto x^{1/3}$ (Chongsiripinyo & Sarkar 2020). Assume that the energetic eddies responsible for wave generation scale with L_{Hk} and that the internal wave radiation becomes significant only when Nt reaches a specific value. Then, the distance at which the internal wave radiation commences scales as Fr, the value of L_{Hk} at that location varies as $Fr^{1/3}$ and, therefore, $\lambda \propto Fr^{1/3}$. Indeed, it will be shown in § 5.3 that the wake-wave potential energy (as a fraction of turbulent kinetic energy of the wake) becomes significant at $Nt \approx 5$ and then does not change appreciably until $Nt \approx 30$ when it decreases.

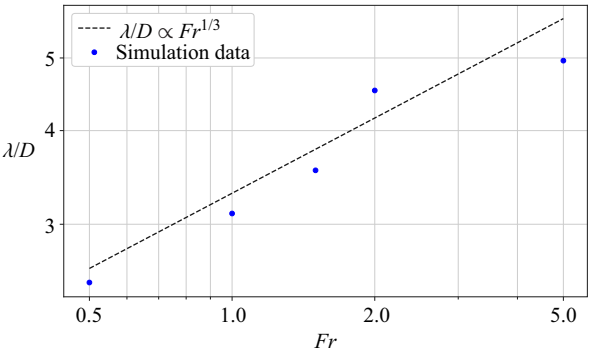

Figure 9. Wavelength of wake-generated internal gravity waves.

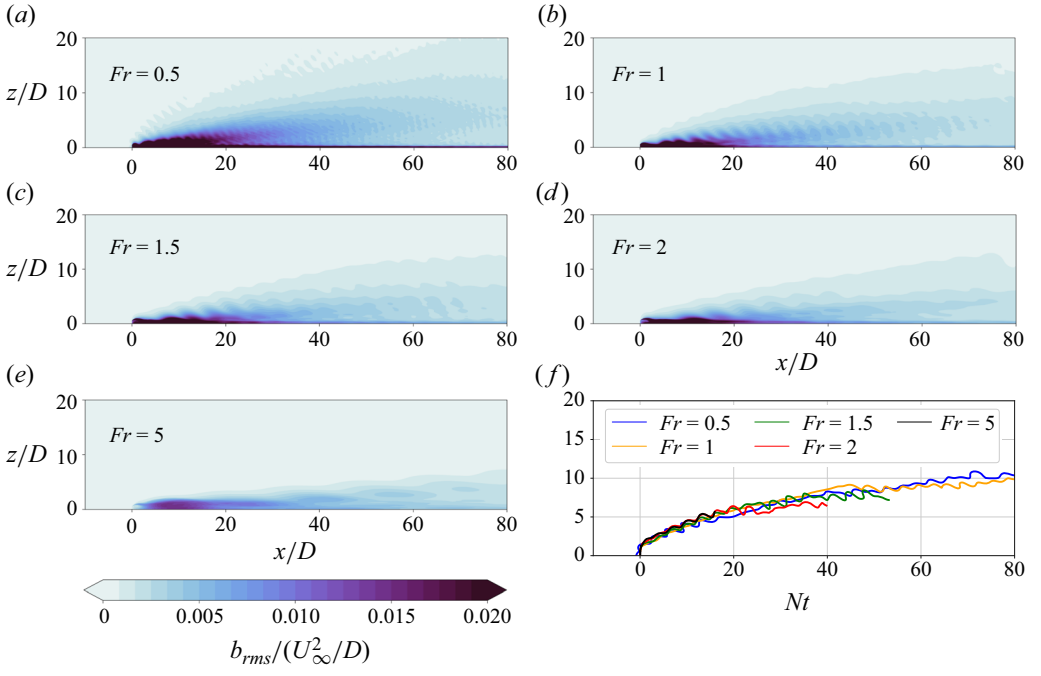

Figure 10. (*a–e*) Wake wave envelope visualised by the root mean square (r.m.s.) of buoyancy term for the five cases. (*f*) Contour lines of $b_{rms} = 0.0015U_\infty^2/D$ plotted with Nt.

Lastly, to explain the trend in vertical extent of the waves, the contours of the r.m.s. buoyancy term $b_{rms} = g\rho_{d_{rms}}/\rho_0$ are plotted in figure 10(*a–e*), thereby providing a good visualisation of the envelope of the wake-generated internal waves. When the vertical extent of this envelope (quantified by a small value of $b_{rms} = 0.0015U_\infty^2/D$) is plotted against Nt in figure 10(*f*), a good collapse is seen, showing that the vertical extent of propagation is the same for these waves in buoyancy time units. For example, $x = 40$ corresponds to $Nt = 80$ for $Fr = 0.5$ and $Nt = 8$ for $Fr = 5$, accounting for the difference in wave envelope between these cases at the same x.

5. Wake and wave energetics

A turbulent stratified flow has both kinetic and potential energy with each having a mean and a fluctuating component. Furthermore, the mean and the fluctuation can be divided into a turbulent wake component and a wave part surrounding the wake component. In this section, the variation of the energy partition among its components will be diagnosed. It will be shown that, across the five levels of stratification, there is a systematic variation of mean relative to turbulent components as well as potential versus kinetic energy. The definitions of various energy components are as follows:

mean kinetic energy,

$$MKE = \tfrac{1}{2}((\langle u\rangle - U_\infty)^2 + \langle v\rangle^2 + \langle w\rangle^2); \tag{5.1}$$

mean potential energy,

$$MPE = \frac{g^2\langle \rho_d\rangle^2}{2\rho_0^2 N^2}; \tag{5.2}$$

turbulent kinetic energy,

$$TKE = \tfrac{1}{2}(\langle u'^2\rangle + \langle v'^2\rangle + \langle w'^2\rangle); \tag{5.3}$$

turbulent potential energy,

$$TPE = \frac{g^2\langle \rho_d'^2\rangle}{2\rho_0^2 N^2}. \tag{5.4}$$

The various plots in this section compare the evolution of these energy components, integrated over the r–θ plane, as a function of streamwise distance (x). Let A be the complete r–θ plane in the simulation domain at any x. If C is a closed curve on A enclosing the area A_C, the following three integrals of a quantity $E(r, \theta, x)$ can be defined as a function of x (see figure 11 for two examples of the curve C chosen to separate the wave from the wake field): Total integral over the complete r–θ plane,

$$E_{TI}(x) = \int_A E(r, \theta, x) r \,\mathrm{d}r \,\mathrm{d}\theta; \tag{5.5}$$

inside integral over the area bounded by C on r–θ plane (note that C varies as a function of x),

$$E_{II}(x) = \int_{A_C(x)} E(r, \theta, x) r \,\mathrm{d}r \,\mathrm{d}\theta; \tag{5.6}$$

outside integral, which is computed over the area external to that bounded by C,

$$E_{OI}(x) = \int_{A-A_C(x)} E(r, \theta, x) r \,\mathrm{d}r \,\mathrm{d}\theta; \tag{5.7}$$

so that, $E_{TI}(x) = E_{II}(x) + E_{OI}(x)$.

5.1. *Mean kinetic energy and mean potential energy*

The curve C in (5.6), and (5.7) will be chosen to be at the edge of the wake so that the outside integral serves as a surrogate for the wave energy and the inside integral for the wake energy. Specifically, an ellipse with its semimajor and semiminor lengths equal to

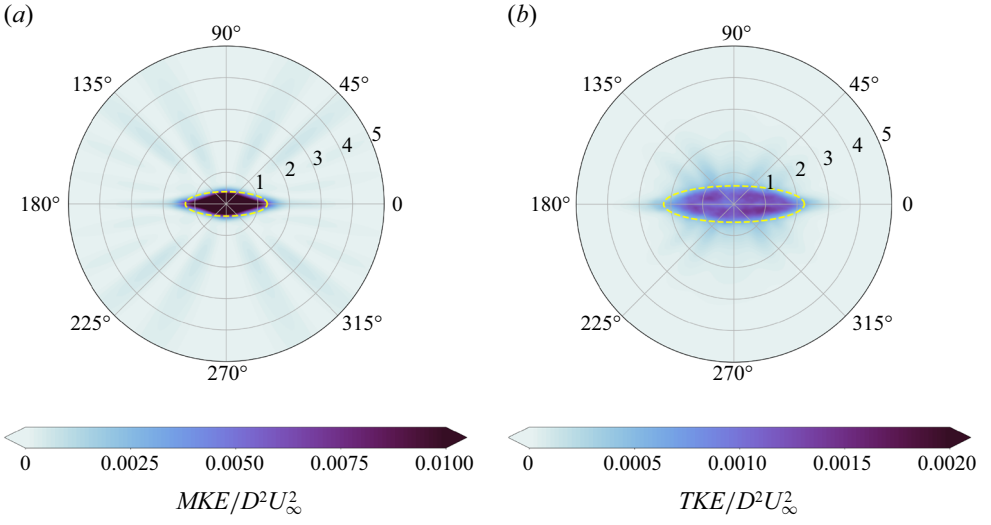

Figure 11. Examples of curve C (here an ellipse shown in dashed yellow line) used to separate the wave from the wake contribution: (a) mean kinetic energy contours for $Fr = 1.5$ at $x/D = 20$ as separated by C based on half-width of wake U_d profile; (b) turbulent kinetic energy contours for $Fr = 1.5$ at $x/D = 20$ as separated by C based on half-width of wake turbulent kinetic energy profile.

the horizontal and vertical half-width of the mean defect velocity profile is chosen for each Fr case; these lengths vary as a function of x. Thus, using (5.5), (5.6) and (5.7), the wake and wave contributions based on the inside and outside regions of the ellipse can be calculated.

Figure 12(a–c) shows the various integrals of MKE for all five cases. For cases with lower Fr, MKE_{TI} (figure 12a) is initially low because of shorter separation zones (see figure 4). However, MKE_{TI} also exhibits slower decay with increasing x for the higher-Fr cases, reflecting the fact that stratification prolongs wake lifetime, so that the Fr variation in MKE_{TI} eventually reverses at later time. There is significant mean kinetic energy in the outside wave region (figure 12c), which can be attributed to the lee waves, except at the highest simulated $Fr = 5$ case with weak lee waves. Moving to mean potential energy shown in the bottom row, comparison of figure 12(e) and figure 12(f) shows that the outside contribution (MPE_{OI}) owing to steady lee waves dominates over the wake contribution (MPE_{II}) over the entire streamwise extent of the flow. Evidently, the turbulent wake does not lead to significant mean distortion of the isopycnals although there is fluctuating distortion leading to turbulent kinetic energy as will be shown shortly. Beyond $x = 10$, both MKE_{TI} and MPE_{TI} decrease with increasing Fr. The decrease is quite substantial from $Fr = 2$ to $Fr = 5$. Note that the energy values are normalised using U_∞ and D. Thus if the increase of Fr is due to a higher flow speed under the same background N, the Fr-related decrease in the dimensional value of energy would be less.

To summarise, the distribution of mean energy associated with stratified flow past a disk is such that almost all of the mean potential energy component resides outside the turbulent wake in the lee wave field. At $Fr = 2$ or less, most of mean kinetic energy resides in the lee wave field in contrast to the higher $Fr = 5$ case where it is the wake that carries most of the mean kinetic energy.

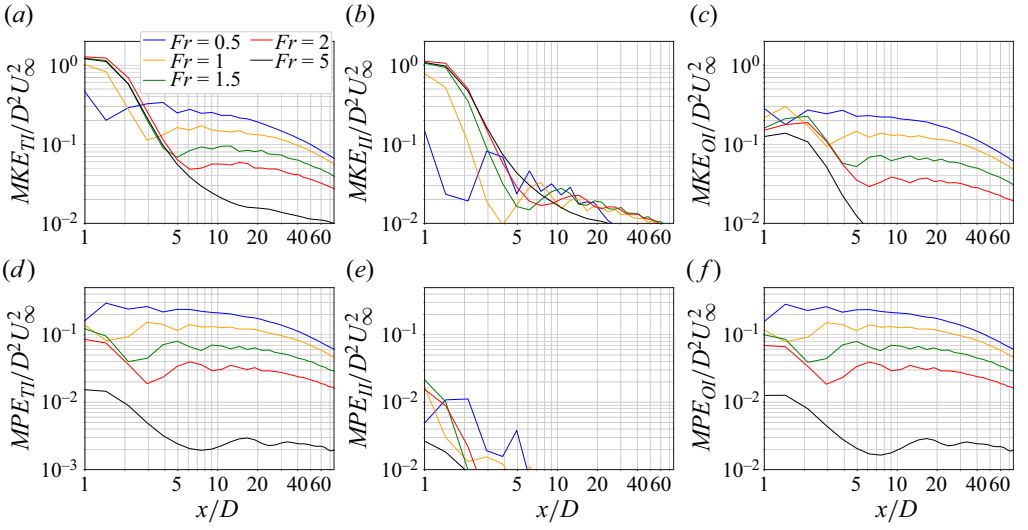

Figure 12. Area-integrated mean energies for all five cases. Total integral (*TI*) of the mean energy is shown as well as its partition into wake or inside integral (*II*) and wave or outside integral (*OI*).

5.2. *Turbulent kinetic energy and turbulent kinetic energy*

Figure 13 shows the various fluctuation energies for all five cases. The fluctuation energy can be divided into the turbulent energy of the wake and the outside fluctuation energy carried by wake-generated internal waves. This is achieved by defining an ellipse with its semimajor and semiminor axes equal to the horizontal and vertical half-width of the turbulent kinetic energy profile, respectively. The various contributions to the turbulent component are plotted similar to what was shown for the mean component in figure 12. Looking at the TKE_{TI} profiles in figure 13(*a*), it is evident that the general Fr-dependence seen in figure 12(*a*) has been flipped, i.e. the total TKE is larger for the cases with larger Fr. Furthermore, the cases with higher Fr also have stronger turbulence as shown by the interior integral TKE_{II} in figure 12(*b*). The exception is the case of $Fr = 0.5$. Here, both TKE_{II} (interior wake turbulence) and TKE_{OI} (external to the wake) flatten at $x \approx 20$, $Nt \approx 40$ and then increase slightly before decaying again. The increase of wake fluctuation energy in the late NEQ/early quasi-two-dimensional regime of the $Fr = 0.5$ case is a result of the wake structure becoming increasingly two-dimensional and its flapping in the horizontal, similar to what was found for $Fr < 1$ sphere wakes at $Re = 3700$ by Pal *et al.* (2016).

The TPE_{TI} for $Fr = 0.5$ also shows slight stalling at $x/D \approx 10$ before decaying again at $x/D \approx 30$, although this is likely the result of internal wave activity in the NEQ regime as can be seen from increase in external fluctuation energy, TPE_{OI} in figure 13(*f*). Comparing figure 13 with figure 12 shows that $Fr = 5$ is qualitatively different than the other four cases, e.g. it has a larger potential energy in the fluctuations than in the mean.

5.3. *Ratio of kinetic and potential energies*

Figure 14 shows the mean and fluctuation energy ratios (MPE_{TI}/MKE_{TI} and TPE_{TI}/TKE_{TI}), respectively, plotted as a function of x/D as well as Nt. For the mean energies, the ratio MPE_{TI}/MKE_{TI} approaches a constant value after $Nt \approx 5$. This constant $O(1)$ value has a small variation for the lower Fr cases, e.g between 0.9 at $Fr = 0.5$ to

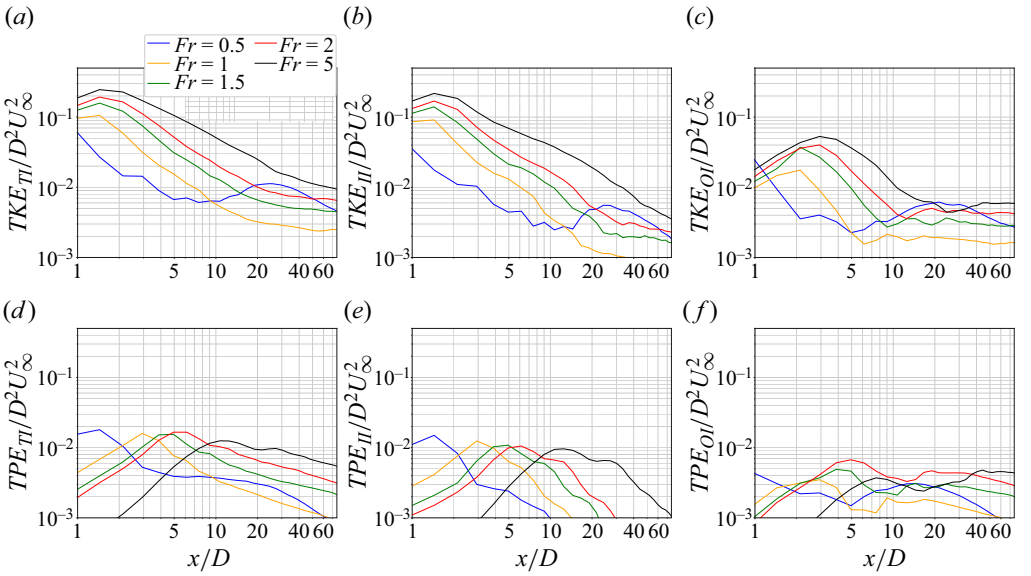

Figure 13. Area integrated fluctuation energies for all five cases. The total integral of the fluctuating energy is shown as well as its partition into wake or inside integral and wave or outside integral.

0.6 at $Fr = 2$. However, there is a large decrease of the ratio to 0.2 at $Fr = 5$, pointing to a decrease in the importance of the lee wave field at high Fr. Insofar as the fluctuation energy ratio, TPE_{TI}/TKE_{TI}, it increases as the wake evolves to approach a plateau at 0.6–0.7 in the region $5 < Nt < 30$ (figure 14*d*). This plateau lies within the NEQ regime where the wake adjusts to the background stratification and the activity of the wake-generated internal waves is the highest.

5.4. *Comparison of body lee wave energy with wake wave energy*

Previous laboratory measurements (Brandt & Rottier 2015; Meunier *et al.* 2018) at selected spatial locations have shown that, while the body wave field is more energetic than the wake wave field at lower Fr, there is a crossover to dominance of wake wave energy at sufficiently large Fr. The wave energy is computed from the outside integral terms, i.e. $E_{body\ wave} = MPE_{OI} + MKE_{OI}$ and $E_{wake\ wave} = TPE_{OI} + TKE_{OI}$. Figure 15 compares the downstream evolution of $E_{body\ wave}$ and $E_{wake\ wave}$. Unlike the behaviour in the lower-Fr cases, the energy in the wake-generated internal waves at at $Fr = 5$ surpasses the energy in steady lee waves. Thus, in the disk wake, a crossover to the dominance of wake waves occurs at a value of Fr between 2 and 5.

6. Comparison with disk wakes at $Re = 50\,000$

In this section, internal waves from the data (Chongsiripinyo & Sarkar 2020) for a disk wake at a higher $Re = 50\,000$ and with $Fr = 2$, 10 are quantified and the results compared with the Fr dependencies discussed in the previous sections.

6.1. *Structure of body-generated lee waves and wake-generated internal gravity waves*

Lee waves for $Re = 5000$ and $Re = 50\,000$ at $Fr = 2$ are compared in figure 16 by plotting vertical velocity (w) contours on the $\theta = 90^\circ$ plane and also the value of w along the line

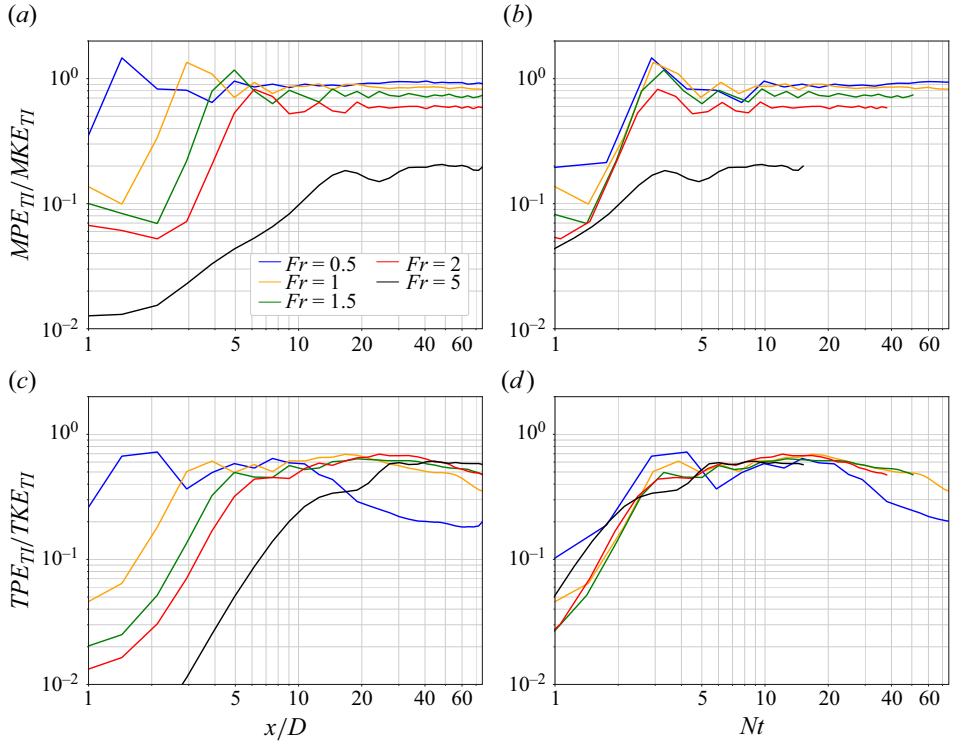

Figure 14. Ratio of potential and kinetic energy for all the five cases. This ratio is plotted for the mean and turbulent components as a function of x/D (*a*,*c*) and Nt (*b*,*d*).

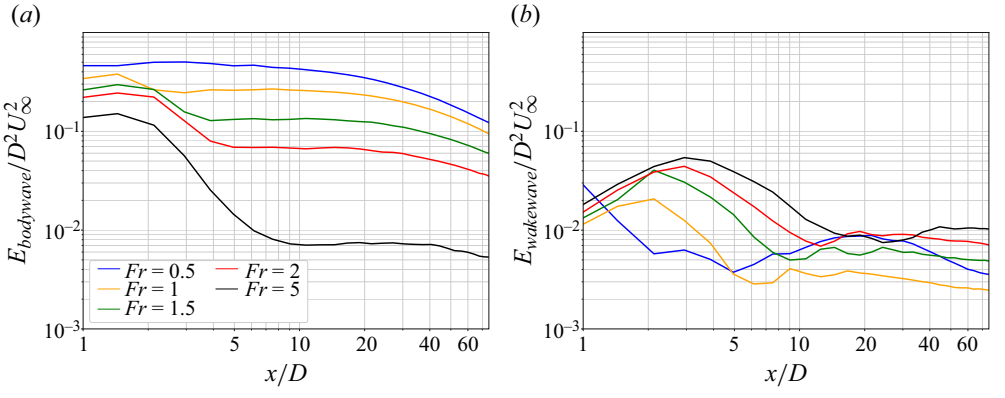

Figure 15. (*a*) Total energy in body lee waves (*b*). Total energy in wake-generated internal waves.

$z = x$, $y = 0$. The influence of Re on the wavelength and spatial distribution of the wave field is negligible. The lee waves for the $Re = 50\,000$ case at $Fr = 10$ (not shown here) are weaker than at $Fr = 2$ and have longer wavelength, in agreement with the linear theory result of § 3.

The influence of Re on wake waves is illustrated by figure 17(*a*,*b*) that shows $\partial w'/\partial z$ on the vertical centre half-plane ($\theta = 90^\circ$). Similarity is observed in the inclination of the waves ($\Theta \approx 40^\circ$) as well as their wavelength ($\lambda/D \approx 4.5$). The $Re = 50\,000$ wake is

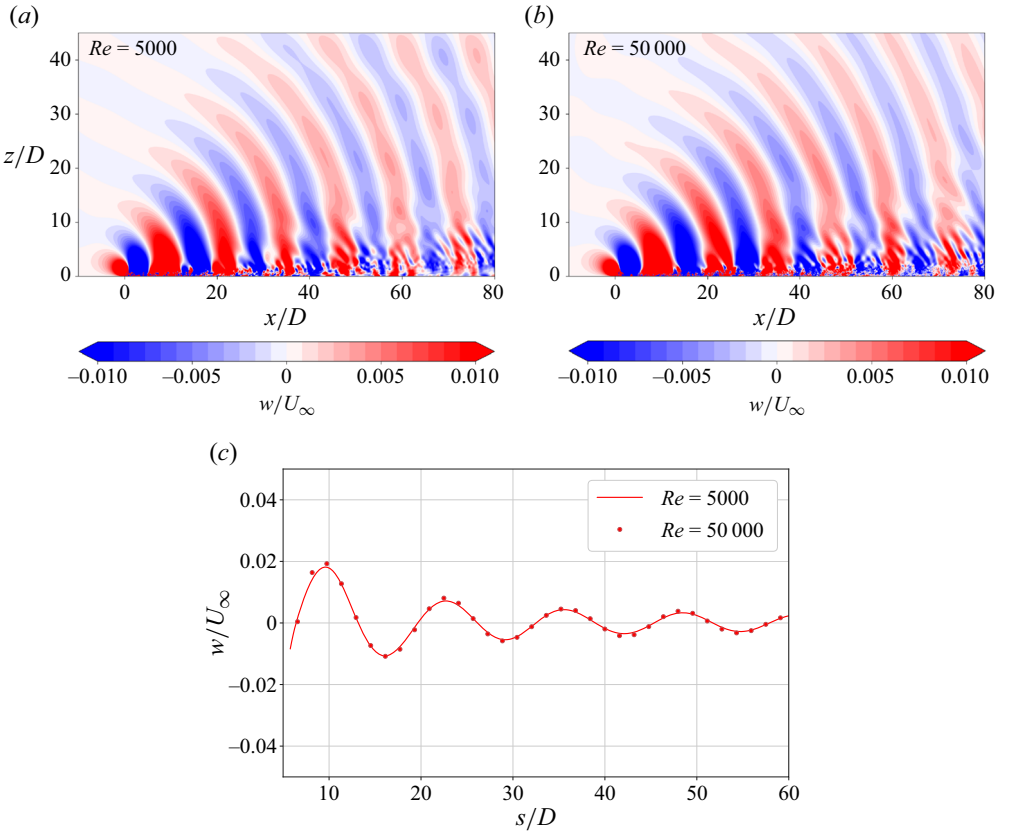

Figure 16. Lee wave comparison for $Re = 5000$ and $Re = 50\,000$ at $Fr = 2$: (*a*,*b*) instantaneous vertical velocity contours; (*c*) vertical velocity on the line $z = x$, $y = 0$ ($s = \sqrt{x^2 + z^2}$).

more turbulent than at $Re = 5000$ as suggested visually by figure 17(*b*) with enhanced small-scale features in the wake core relative to 17(*a*).

The wake wave amplitude, measured by $(\partial w'/\partial z)_{rms}$, is compared between $Re = 5000$ and $Re = 50\,000$ in figure 17(*c*,*d*). Proximity to the wake leads to a higher difference in wave amplitude, as is observed at $z/D = 2$ relative to $z/D = 4$. The scales of wake structures that give rise to wake waves are more broadband for $Re = 50\,000$ as compared with $Re = 5000$ and at higher Re, waves are less affected initially by viscosity.

Meunier *et al.* (2018) report an empirical scaling of $Re^{0.4}$ for the wake wave amplitude and Abdilghanie & Diamessis (2013) report that wave momentum flux varies as $\langle uw \rangle \sim Re^{0.25}$. Since the increase of wave amplitude with Re depends on streamwise location in the present simulations, we refrain from proposing a power law dependence on Re.

6.2. *Plane-integrated wave energy*

Analysis of the $Re = 5000$ results showed that when Fr is increased, the total energy in wake waves progressively increases while the total energy in body waves decreases. Those results also showed that at $Fr = 5$, the wake wave energy overtook the body wave energy. Figure 18(*a*,*b*) shows the downstream variation of body wave energy ($E_{body\ wave} = MPE_{OI} + MKE_{OI}$) and wake wave energy ($E_{wake\ wave} = TPE_{OI} + TKE_{OI}$), after including the additional results for $Re = 50\,000$ at $Fr = 2$, 10 to the $Re = 5000$ cases.

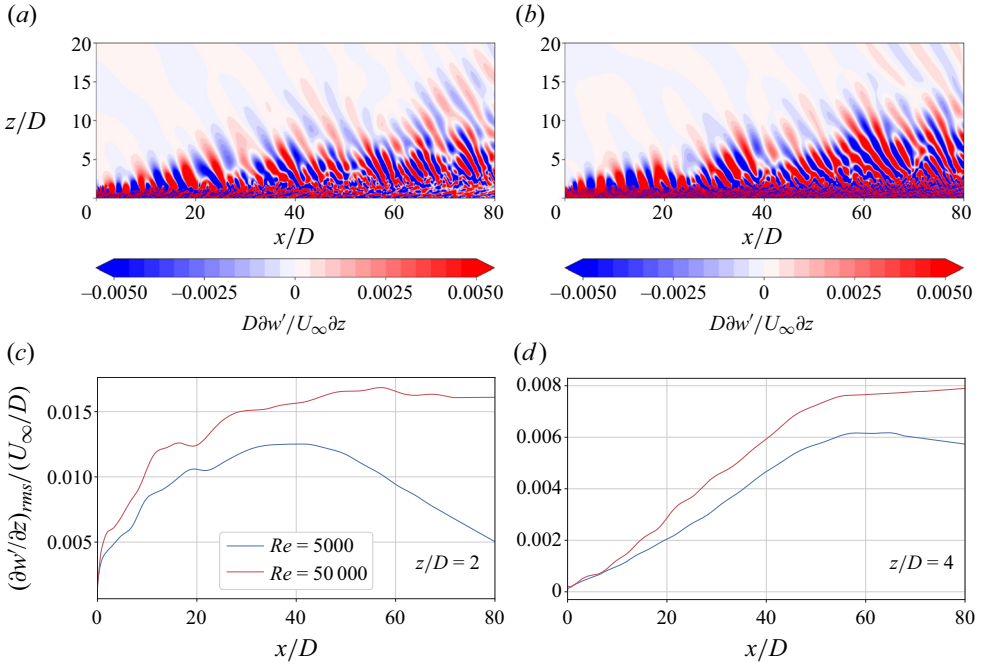

Figure 17. Wake-generated internal wave comparison for (*a*) $Re = 5000$ and (*b*) $Re = 50\,000$ at $Fr = 2$.

The streamwise evolution of $E_{body\ wave}$ at $Fr = 2$ is qualitatively similar between the two values of Re although the values are slightly larger at the higher Re. The $Fr = 10$ case in figure 18(*a*) has the weakest stratification and also the smallest body wave energy among all the simulations, which is consistent with the trend at $Re = 5000$. Turning to the wake wave energy as a function of x/D, the $Fr = 2$ case shows consistently higher wave energy at $Re = 50\,000$ relative to the lower-Re case.

When the ratio TPE_{TI}/TKE_{TI} is plotted against Nt in figure 18(*c*), now also including the data for $Re = 50\,000$, the two new cases also show that the ratio increases as a function of Nt until reaching a maximum value of 0.6–0.7 in the NEQ region, $5 < Nt < 30$. This implies that the balance between the turbulent energies for a stratified flow evolves in a similar fashion not only across different Fr for a fixed Re, but also for higher Re, pointing towards a potential universality of this statistic for stratified flows.

7. Summary and discussion

Body-inclusive LES are used to study the effect of changing stratification levels in flow past a disk. The focus is on internal gravity waves. Systematic investigation of internal waves over a range of Fr is new insofar as body-inclusive simulations and adds to our knowledge base from previous experiments, temporal-model simulations and theory. Linear stratification at five different levels is considered: $Fr = 0.5$, 1, 1.5, 2 and 5 and the flow is quantified up to a relatively long streamwise distance of $x/D = 80$. The Reynolds number based on the free stream velocity (U_∞) and disk diameter (D) is fixed at 5000 and, thus, variability across these cases can be attributed to Fr alone. The dataset of Chongsiripinyo & Sarkar (2020) for a disk at $Re = 50\,000$ at $Fr = 2$, 10 is also analysed for studying Reynolds number dependence.

The questions posed in § 1.5 are answered and discussed below.

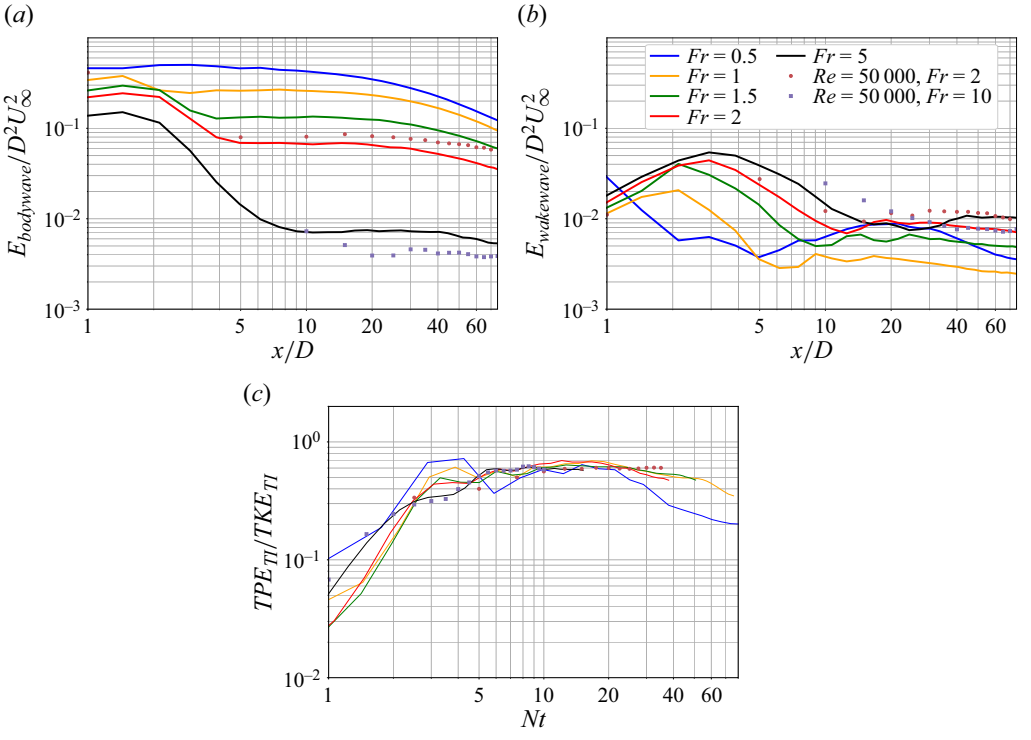

Figure 18. (*a*) Total energy in body lee waves. (*b*) Total energy in wake waves. (*c*) Ratio of total turbulent potential energy and turbulent kinetic energy.

7.1. *Prediction of lee waves*

With regards to the steady lee waves, the non-dimensional amplitude (w) of the vertical velocity decreases with increasing Fr. All five cases showed excellent agreement with the linear theory for steady lee waves by Voisin (2007) when an equivalent body including the separation bubble was used to calculate the potential flow solution. As to the separation bubble, its length differed considerably among the $Fr = 0.5$, 1 and 1.5 cases but not so much between $Fr = 2$ and $Fr = 5$. According to linear theory (3.3*a*,*b*), $w/U_\infty \propto Fr^{-1}$ if m is constant and the change of m adds some variability. The wavelength (Λ) was found to increase linearly with Fr according to $\Lambda/D \sim 6.7Fr$, close to the asymptotic relation of $\Lambda/D = 2\pi Fr$. The amplitude of mean $\partial w/\partial z$, which was obtained by Meunier *et al.* (2018) in laboratory experiments, was compared with the present simulation results and good mutual agreement was found. The theory proposed by Meunier *et al.* (2018) involves a forcing of the momentum conservation equation (to model the drag) as the leading-order contribution to wave generation while the theory of Voisin (2007) that was adapted for the present application is different and involves a volumetric forcing of the continuity equation. Our adaptation of the theory involves the inclusion of the separation bubble, whose size is related to and generally increases with the drag force, as part of the wave forcing. Thus, although not equivalent, both the theory used here and that used by Meunier *et al.* (2018) lead to higher wave amplitude for blunter body shapes.

7.2. *Properties of wake waves*

Unlike the body-attached lee waves, the wake waves advect downstream with respect to the disk. In a reference frame moving with the free stream, the wake waves move

upstream consistent with the notion that the wake has a velocity deficit with respect to the free stream. A narrow band ($\Theta = 35^\circ$–40° with respect to the vertical) is found for the wave propagation angles for all the five Fr cases. Narrow-band emission from turbulent shear flows has been found previously, e.g. from a shear layer (laboratory experiments by Sutherland & Linden (1998) and DNS by Pham *et al.* (2009)), a turbulent Ekman layer (Taylor & Sarkar 2007) and temporal-model simulations of a wake (Abdilghanie & Diamessis 2013). The wave propagation angles observed here are consistent with the analytical result of 35° that follows from the vertical group velocity maximisation (equivalently, viscous decay minimisation) criterion given by Taylor & Sarkar (2007). It is worth noting that Abdilghanie & Diamessis (2013) found that the narrow band in their lower Re cases expanded to a wider band of inclination angles (26°–50°) at higher Re; a possible reason is the reduced effect of viscosity on the waves.

Other characteristics of the wake waves were studied as well. The wavelength of these waves increases with an increase in Fr, agreeing well with the $\lambda \propto Fr^{1/3}$ scaling found by Abdilghanie & Diamessis (2013) and Meunier *et al.* (2018). Also, the wavelength remains approximately constant until the end of the test domain at $x = 80$. The horizontal width of the turbulent kinetic energy profile increases as $x^{1/3}$ and the wave potential energy as a fraction of turbulent kinetic energy becomes significant at $Nt = Nx/U_\infty \approx 5$ for all five cases. Thus, the streamwise distance at which the internal wave burst becomes significant scales as Fr, the length scale of the energetic flow structures (same order as the turbulent kinetic energy profile thickness) at that point scales as $Fr^{1/3}$, and so does the corresponding wavelength of the radiated internal wave.

The envelope of the wake waves is quantified by choosing the r.m.s. value of the buoyancy at the envelope boundary to be a small fixed value. The width of the thus defined envelope at a given x expands with decreasing Fr. Nevertheless, self-similar evolution is found when the wave envelope is plotted as a function of the buoyancy time scale (Nt). The use of Nt in place of x/D is necessary because the evolution time scale of wake waves is a buoyancy effect that depends on stratification ($1/N$) and not on advection (D/U_∞).

7.3. *Wave and wake energetics*

Because of the presence of both a turbulent wake and internal gravity waves external to the wake, it makes sense to partition the energies in the flow into their respective interior (wake) and exterior (wave) contributions. This is done by calculating the area integrals of the energy which are then segregated into their wake and wave parts. The interior wake part of the energy is defined to be inside an ellipse whose dimensions are determined by the x-dependent values of the vertical and horizontal half-widths of the wake and the exterior wave part is the remaining portion. The wake–wave decomposition is applied to the kinetic energy (both the mean component, MKE, and the turbulent component, TKE) and the potential energy (mean component, MPE, and turbulent component, TPE).

Comparison of the body lee wave energy (outside integrals of mean energies) and wake wave energy (outside integrals of fluctuation energies) shows that lee waves are a dominant feature for lower $Fr \sim O(1)$ while unsteady wake waves become more significant as Fr is increased. For the disk wake, $Fr = 2$ is below the crossover and $Fr = 5$ is above the crossover point at which both types of waves have similar energetic importance. The crossover from lee-wave dominance to wake-wave dominance at sufficiently large Fr has been seen at selected measurement stations in previous experimental studies, e.g. Brandt & Rottier (2015) and Meunier *et al.* (2018).

For the mean flow, it is found that although mean kinetic energy gets its contribution from both the wake defect and the lee waves, mean potential energy is primarily in the lee waves with $Fr = 0.5$ having the highest value. Beyond the near wake, the wake contribution to mean kinetic energy increases with a decrease in Fr, i.e. strengthening stratification, consistent with stratification prolonging the lifetime of the wake. The ratio of total mean potential energy to total mean kinetic energy reaches a case-dependent constant value beyond $Nt \approx 5$ that decreases with increasing Fr. The ratio takes higher values of 0.6 –1 at Fr between 0.5 and 2 – the regime where lee waves dominate over wake waves.

For the fluctuation energies, $Fr = 5$ has the highest wake turbulent kinetic energy. Notably, the ratio of turbulent potential energy and turbulent kinetic energy exhibits a universal trend based on all the cases considered in this study, where it is seen to have a constant value of 0.6 to 0.7 for $5 < Nt < 40$, which coincides with the NEQ regime, wherein the wake-generated internal wave activity is the highest as part of the adjustment of the wake turbulence to the background stratification.

7.4. *Effect of increasing Reynolds number*

Using the dataset of Chongsiripinyo & Sarkar (2020), it was established that the increase in Reynolds number has little effect on lee wave properties such as wavelength and amplitude. However, the amplitude of wake waves, measured by pointwise values of $(\partial w'/\partial z)_{rms}$, increases with Re. The relative enhancement of wave energy is higher at locations closer to the wake. The increase of wake wave amplitude with increasing Re is consistent with previous results (Abdilghanie & Diamessis 2013; Meunier *et al.* 2018). Importantly, the ratio of cross-sectional areas of turbulent potential energy and turbulent kinetic energy exhibits some universality. Specifically, the peak value of this ratio takes the value 0.6–0.7 in the NEQ regime for all Re and Fr cases in this study.

7.5. *Limitations and outlook*

Internal waves are examined in this study with body-inclusive simulations for Fr between 0.5 and 10. It is of interest to expand the parameter space to $Fr > 10$, a regime with initially weak buoyancy effects, and test the present scaling laws on wake wave structure and energetics. At such high values of Fr, a large streamwise domain with $x/D = FrNt$ is required to capture the regime ($5 < Nt < 40$) that has energetic internal waves. The robustness of the present results at higher Re also deserves further study. A pure body-inclusive approach with the long streamwise domains required at high Fr or the fine grid spacing required at high Re would incur excessively high computational cost. The hybrid approach, which combines a body-inclusive simulation with a body-exclusive simulation (either spatial or temporal), is a good option to extend the Fr and Re range of simulations.

Supplementary material. Supplementary movies are available at https://doi.org/10.1017/jfm.2024.717.

Funding. The authors gratefully acknowledge the support of Office of Naval Research, grant no. N00014-20-1-2253.

Declaration of interests. The authors report no conflict of interest.

Author ORCIDs.
D. Gola https://orcid.org/0009-0002-4377-4850;
S. Nidhan https://orcid.org/0000-0003-0433-6129;
S. Sarkar https://orcid.org/0000-0002-9006-3173.

References

ABDILGHANIE, A.M. & DIAMESSIS, P.J. 2013 The internal gravity wave field emitted by a stably stratified turbulent wake. *J. Fluid Mech.* **720**, 104–139.

BALARAS, E. 2004 Modeling complex boundaries using an external force field on fixed Cartesian grids in large-eddy simulations. *Comput. Fluids* **33** (3), 375–404.

BONNETON, P., CHOMAZ, J.M. & HOPFINGER, E.J. 1993 Internal waves produced by the turbulent wake of a sphere moving horizontally in a stratified fluid. *J. Fluid Mech.* **254**, 23–40.

BONNIER, M. & EIFF, O. 2002 Experimental investigation of the collapse of a turbulent wake in a stably stratified fluid. *Phys. Fluids* **14** (2), 791–801.

BRANDT, A. & ROTTIER, J.R. 2015 The internal wavefield generated by a towed sphere at low Froude number. *J. Fluid Mech.* **769**, 103–129.

BRUCKER, K.A. & SARKAR, S. 2010 A comparative study of self-propelled and towed wakes in a stratified fluid. *J. Fluid Mech.* **652**, 373–404.

CASTRO, I.P., SNYDER, W.H. & MARSH, G.L. 1983 Stratified flow over three-dimensional ridges. *J. Fluid Mech.* **135**, 261–282.

CHOMAZ, J.M., BONNETON, P. & HOPFINGER, E.J. 1993 The structure of the near wake of a sphere moving horizontally in a stratified fluid. *J. Fluid Mech.* **254**, 1–21.

CHONGSIRIPINYO, K. & SARKAR, S. 2020 Decay of turbulent wakes behind a disk in homogeneous and stratified fluids. *J. Fluid Mech.* **885**, A31.

DIAMESSIS, P.J., SPEDDING, G.R. & DOMARADZKI, J.A. 2011 Similarity scaling and vorticity structure in high-Reynolds-number stably stratified turbulent wakes. *J. Fluid Mech.* **671**, 52–95.

DOMMERMUTH, D.G., ROTTMAN, J.W., INNIS, G.E. & NOVIKOV, E.A. 2002 Numerical simulation of the wake of a towed sphere in a weakly stratified fluid. *J. Fluid Mech.* **473**, 83–101.

GARRETT, C. & KUNZE, E. 2007 Internal tide generation in the deep ocean. *Annu. Rev. Fluid Mech.* **39**, 57–87.

GERMANO, M., PIOMELLI, U., MOIN, P. & CABOT, W.H. 1991 A dynamic subgridscale-scale eddy viscosity model. *Phys. Fluids* **3** (7), 1760–1765.

GILREATH, H.E. & BRANDT, A. 1985 Experiments on the generation of internal waves in a stratified fluid. *AIAA J.* **23** (5), 693–700.

GOLA, D., NIDHAN, S., ORTIZ-TARIN, J.L., PHAM, H.T. & SARKAR, S. 2023 Disk wakes in nonlinear stratification. *J. Fluid Mech.* **956**, A5.

GOURLAY, M.J., ARENDT, S.C., FRITTS, D.C. & WERNE, J. 2001 Numerical modeling of initially turbulent wakes with net momentum. *Phys. Fluids* **13** (12), 3783–3802.

HANAZAKI, H. 1988 A numerical study of three-dimensional stratified flow past a sphere. *J. Fluid Mech.* **192**, 393–419.

HUNT, J.C.R. & SNYDER, W.H. 1980 Experiments on stably and neutrally stratified flow over a model three-dimensional hill. *J. Fluid Mech.* **96** (4), 671–704.

JACOBITZ, F.G., SARKAR, S. & VANATTA, C.W. 1997 Direct numerical simulations of the turbulence evolution in a uniformly sheared and stably stratified flow. *J. Fluid Mech.* **342**, 231–261.

LILLY, D.K. 1992 A proposed modification of the germano sugrid-scale closure method. *Phys. Fluids* A **4**, 633–635.

LIN, J.T. & PAO, Y.H. 1979 Wakes in stratified fluids. *Annu. Rev. Fluid Mech.* **11** (1), 317–338.

LIN, Q., BOYER, D.L. & FERNANDO, H.J.S. 1992 Turbulent wakes of linearly stratified flow past a sphere. *Phys. Fluids* **4** (8), 1687–1696.

MENEVEAU, C., LUND, T.S. & CABOT, W.H. 1996 A lagrangian dynamic subgrid-scale model of turbulence. *J. Fluid Mech.* **319**, 353–385.

MEUNIER, P., LE DIZÈS, S., REDEKOPP, L. & SPEDDING, G.R. 2018 Internal waves generated by a stratified wake: experiment and theory. *J. Fluid Mech.* **846**, 752–788.

NIDHAN, S., CHONGSIRIPINYO, K., SCHMIDT, O.T. & SARKAR, S. 2020 Spectral proper orthogonal decomposition analysis of the turbulent wake of a disk at $Re = 50\,000$. *Phys. Rev. Fluids* **5** (12), 124606.

NIDHAN, S., SCHMIDT, O.T. & SARKAR, S. 2022 Analysis of coherence in turbulent stratified wakes using spectral proper orthogonal decomposition. *J. Fluid Mech.* **934**, A12.

ORLANSKI, I. 1976 A simple boundary condition for unbounded hyperbolic flows. *J. Comput. Phys.* **21** (3), 251–269.

ORR, T.S., DOMARADZKI, J.A., SPEDDING, G.R. & CONSTANTINESCU, G.S. 2015 Numerical simulations of the near wake of a sphere moving in a steady, horizontal motion through a linearly stratified fluid at $Re = 1000$. *Phys. Fluids* **27** (3), 035113.

ORTIZ-TARIN, J.L., CHONGSIRIPINYO, K.C. & SARKAR, S. 2019 Stratified flow past a prolate spheroid. *Phys. Rev. Fluids* **4** (9), 094803.

PAL, A., SARKAR, S., POSA, A. & BALARAS, E. 2016 Regeneration of turbulent fluctuations in low-Froude number flow over a sphere at Reynolds number of 3700. *J. Fluid Mech.* **804 R2**, 1–11.

PAL, A., SARKAR, S., POSA, A. & BALARAS, E. 2017 Direct numerical simulation of stratified flow past a sphere at a subcritical Reynolds number of 3700 and moderate Froude number. *J. Fluid Mech.* **826**, 5–31.

PASQUETTI, R. 2011 Temporal/spatial simulation of the stratified far wake of a sphere. *Comput. Fluids* **40** (1), 179–187.

PHAM, H.T., SARKAR, S. & BRUCKER, K.A 2009 Dynamics of a stratified shear layer above a region of uniform stratification. *J. Fluid Mech.* **630**, 191–223.

REDFORD, J.A., LUND, T.S. & COLEMAN, G.N. 2015 A numerical study of a weakly stratified turbulent wake. *J. Fluid Mech.* **776**, 568–609.

REDFORD, J.A., CASTRO, I.P. & COLEMAN, G.N. 2012 On the universality of turbulent axisymmetric wakes. *J. Fluid Mech.* **710**, 419–452.

ROBEY, H.F. 1997 The generation of internal waves by a towed sphere and its wake in a thermocline. *Phys. Fluids* **9** (11), 3353–3367.

ROWE, K.L., DIAMESSIS, P.J. & ZHOU, Q. 2020 Internal gravity wave radiation from a stratified turbulent wake. *J. Fluid Mech.* **888**, A25.

SARKAR, S. & SCOTTI, A. 2017 From topographic internal gravity waves to turbulence. *Ann. Rev. Fluid Mech.* **49**, 195–220.

SPEDDING, G.R. 1997 The evolution of initially turbulent bluff-body wakes at high internal Froude number. *J. Fluid Mech.* **337**, 283–301.

SPEDDING, G.R. 2001 Anisotropy in turbulence profiles of stratified wakes. *Phys. Fluids* **13** (8), 2361–2372.

SPEDDING, G.R., BROWAND, F.K. & FINCHAM, A.M. 1996 Turbulence, similarity scaling and vortex geometry in the wake of a towed sphere in a stably stratified fluid. *J. Fluid Mech.* **314**, 53–103.

DE STADLER, M.B. & SARKAR, S. 2012 Simulation of a propelled wake with moderate excess momentum in a stratified fluid. *J. Fluid Mech.* **692**, 28–52.

SUTHERLAND, B.R. & LINDEN, P.F. 1998 Internal wave excitation from stratified flow over a thin barrier. *J. Fluid Mech.* **377**, 223–252.

TAYLOR, J.R. & SARKAR, S. 2007 Internal gravity waves generated by a turbulent bottom ekman layer. *J. Fluid Mech.* **590**, 331–354.

VANDINE, A., CHONGSIRIPINYO, K. & SARKAR, S. 2018 Hybrid spatially-evolving DNS model of flow past a sphere. *Comput. Fluids* **171**, 41–52.

VOISIN, B. 1991 Internal wave generation in uniformly stratified fluids. Part 1. Green's function and point sources. *J. Fluid Mech.* **231**, 439–480.

VOISIN, B. 2003 Limit states of internal wave beams. *J. Fluid Mech.* **496**, 243–293.

VOISIN, B. 2007 Lee waves from a sphere in a stratified flow. *J. Fluid Mech.* **574**, 273–315.

WATANABE, T., RILEY, J.J., NAGATA, K., ONISHI, R. & MATSUDA, K. 2018 A localized turbulent mixing layer in a uniformly stratified environment. *J. Fluid Mech.* **849**, 245–276.

WUNSCH, C. & FERRARI, R. 2004 Vertical mixing, energy, and the general circulation of the oceans. *Annu. Rev. Fluid Mech.* **36**, 281–314.

YANG, J. & BALARAS, E. 2006 An embedded-boundary formulation for large-eddy simulation of turbulent flows interacting with moving boundaries. *J. Comput. Phys.* **215** (1), 12–40.

ZHOU, Q. & DIAMESSIS, P.J. 2019 Large-scale characteristics of stratified wake turbulence at varying Reynolds number. *Phys. Rev. Fluids* **4** (8), 084802.